New insight into heterointerfacial effect for heterogenized metallomacrocycle catalysts in executing electrocatalytic CO_2 reduction

Meng-Ke Hu [a,1], Shenghua Zhou [a,c,1], Dong-Dong Ma [a,*], Qi-Long Zhu [a,b,c,*]

[a] State Key Laboratory of Structural Chemistry, Fujian Institute of Research on the Structure of Matter Chinese Academy of Sciences (CAS), Fuzhou 350002, China
[b] Fujian Science & Technology Innovation Laboratory for Optoelectronic Information of China, Fuzhou 350108, China
[c] University of Chinese Academy of Sciences, Beijing 100049, China

ARTICLE INFO

ABSTRACT

The heterogenized metallomacrocycles with atomically dispersed active sites are identified as the promising candidates for electrocatalytic CO_2 reduction reaction (CO_2RR), where their unique heterointerface with interaction between sp^2 carbon and macrocyclic molecules is important but remains vague. Herein, based on well-structured nickel phthalocyanine and porphyrin with the same functional groups (MeNiPc and MeNiPp), the influences of heterointerfacial effect on catalytic performances are systematically disclosed. Through the molecular structure-induced self-adaptive adsorption with optimized heterointerfacial distance, MeNiPc/graphene reveals a high CO Faradaic efficiency of ~99% in a wide potential window, greatly outperforming the MeNiPp/graphene counterpart ($\leq$29.6%). Detailed measurements and theoretical calculations decipher that the higher CO_2RR activity of MeNiPc/graphene is attributed to the unique electronic structures of the Ni-N_4 configurations suitable for well-suited heterointerfacial charge transfer and rapid CO desorption. Additionally, the extended research confirms the universality of heterointerface engineering on boosting the catalytic performances.

1. Introduction

How to reduce carbon dioxide (CO_2) emissions into the atmosphere and convert them into carbon-neutral high-energy-density fuels and valuable chemical feedstocks is crucial for human survival and sustainable development [1–4]. Due to the operability under ambient temperature and pressure, electrocatalytic reduction of CO_2 is recognized as an attractive avenue to mitigate these problems and maintain the carbon-neutral cycle [5–8]. At present, many electrocatalysts have been extensively developed to explore conversion of CO_2 in aqueous medium, such as metals/alloys [9–11], molecules [12–16], framework materials and so on [17–19]. Specifically, molecule-based electrocatalysts show enormous advantages in CO_2 conversion efficiency and atomic economy [20,21]. However, molecular catalysts also face some challenges due to their weak electrical conductivity and strong aggregation tendency. Luckily, combining the homogeneity of the catalytic sites with the conductivity of the substrates (especially sp^2 pattern carbons) provides a promising route for electrocatalytic CO_2 reduction reaction (CO_2RR), because the immobilized molecular catalysts not only

possess well-defined structures to tune performance on the molecular or atomic perspective, but also show the heterogenization of the homogeneous catalysts with high activity, selectivity and stability, and good recycling [21–26]. Among a diversity of molecule-based immobilized electrocatalysts, the heterogenized metallomacrocycles (e.g., phthalocyanines and porphyrins) with the well-defined metal-nitrogen coordination structures have proven high catalytic properties for CO_2RR owing to their conjugated coordination structures enhancing their own implantation effect, the overall electron transport capacity and delocalized electron density [27–31]. Meanwhile, in-depth understandings of the controllable effects for CO_2RR performance in single-molecularly immobilized catalysts were also studied [32–39]. For example, through changing the functional groups (electron-donating amino and electron-withdrawing nitro) around cobalt phthalocyanine (CoPc), Ren et al. prepared a series of single Co atom electrocatalysts. They verified that the electron-withdrawing functional groups can promote CO_2 reduction to CO at a high Faradaic efficiency (FE) [36]. Wang group studied two conjugated N_4-macrocyclic Co complexes with different N types and showed that the pyridine N derived Co complex delivers the

---

higher activity for CO_2-to-CO conversion with a FE of 96% compared to pyrrole N derived Co macrocyclic compound [37]. Moreover, for the single-molecularly immobilized catalysts, the metallomacrocycles are generally stabilized with the π-π stacking and charge transfer interactions between them and the sp^2 carbon substrates [1,20,32], and thus the heterointerface and the related distance could significantly modulate the electronic structures of the metal centers in molecules and their interaction with the substrates, which, however, is still lacking of systematic research. Consequently, how to intellectually design and effectively construct the heterointerface with optimal distance is important for understanding the inherent structure-activity relationship of the heterogenized molecular catalysts and boosting their CO_2RR performance for industrial application.

In this work, we firstly designed and synthesized two metallomacrocycles, i.e., a Ni phthalocyanine and a Ni tetraphenyl porphyrin with the same functional group, separately immobilized on graphene (MeNiPc/G and MeNiPp/G), which offer an ideal platform to systematically comprehend the relationship between the heterointerfacial effect and the catalytic activity of the heterogenized metallomacrocycles in electrochemical CO_2 conversion. The MeNiPc/G composite exhibits preeminent electrocatalytic CO_2RR performance with much higher selectivity (ca. 99.4% of FE_{CO}), larger current density, longer periods of stability, as compared to the MeNiPp/G counterpart. Transmission electron microscopy (TEM), UV-Vis and X-ray photoelectron spectroscopy (XPS) measurements suggest that their different molecular structures lead to the distinction of heterointerfacial effects. Particularly, theoretical calculations further disclose that the outstanding CO_2RR activity of MeNiPc/G is attributed to the heterointerface-modulated electronic structures of the centrical Ni-N_4 sites in the immobilized Ni phthalocyanine and enhanced charge transfer interactions induced by the optimized heterointerface and interface-regulated CO desorption beneficial to the CO_2RR kinetics. Besides, the extended research on other metallomacrocycles also suggest that the heterointerfacial effect is not negligible.

2. Experimental

2.1. Materials and reagents

Graphene powder (G, Shandong Yuhuang New Energy Technology Co. Ltd, China), 1,8-diazabicyclo-(5,4,0)-undec-7-ene (DBU) (99%, Aladdin, China), 4-nitrophthalonitrile (98%, Aladdin, China), nickel (II) acetate tetrahydrate ($(CH_3COO)_2Ni·4 H_2O$, 98%, Sinopharm Chemical Reagent, China), 4-tert-butylphenol (99%, Adamas, China), 4-hydroxy-benzoic acid methyl ester (99%, Adamas, China), methyl 4-formylbenzoate (98%, Adamas, China), 4-tert-butylbenzaldehyde (98%, Adamas, China), pyrrole (99%, Adamas, China), dimethyl Sulfoxide-D6 (99.9%, Adamas, China), Chloroform-D (99.9%, Adamas, China), Nafion D-520 dispersion (Alfa Aesar).

2.2. Synthesis of phthalocyanines and porphyrins

2.2.1. Synthesis of 4-methoxycarbonyl-phenoxy phthalonitrile (Me-CN₂)

The compound Me-CN_2 was synthesized by the similar method in literature [33]. 4-Hydroxybenzoic acid methyl ester (1.85 g, 12.0 mmol) and anhydrous K_2CO_3 (4.23 g, 30.0 mmol) were successively added and then stirred in dry-treated N,N-dimethylformamide (25 mL) at 25 °C for 5 h. Thereafter, 4-nitrophthalonitrile (1.77 g, 10.0 mmol) was slowly fed and endlessly stirred until completion of the reaction, which was tracked by thin layer chromatography (TLC). Then, the reaction mixtures were breathed into 100 mL of cold water. The white precipitate was filtrated and elutriated with deionized water for many times. Yield: 82.4%. ^{1}H NMR based on CDCl₃, δ/ppm: 8.14–8.16 (d, 2 H, Aromatic ring-H), 7.76–7.79 (d, 1 H, Aromatic ring-H), 7.35–7.36 (d, 1 H, Aromatic ring-H), 7.28–7.31 (m, 1 H, Aromatic ring-H), 7.12–7.14 (d, 2 H, Aromatic ring-H), 3.95 (s, 3 H, -CH₃).

2.2.2. Synthesis of 4-tert-butylphenoxy phthalonitrile (Tb-CN₂)

The compound Tb-CN_2 was synthesized through the similar processes to Me-CN_2. 4-Tert-butylphenol (4.55 g, 30 mmol), anhydrous K_2CO_3 (8.46 g, 60.0 mmol), and 4-nitrophthalonitrile (1.77 g, 10.0 mmol) were correspondingly hired. After completion of the reaction, the reaction mixtures were breathed into 100 mL of cold water. The white precipitate was filtrated and elutriated with deionized water for many times. Yield: 89.0%. ^{1}H NMR based on CDCl₃, δ/ppm: 7.70–7.72 (d, 1 H, Aromatic ring-H), 7.46–7.48 (d, 2 H, Aromatic ring-H), 7.26 (s, 1 H, Aromatic ring-H), 7.24 (s, 1 H, Aromatic ring-H), 6.98–7.01 (d, 2 H, Aromatic ring-H), 1.36 (s, 9 H, -(CH₃)₃).

2.2.3. Synthesis of tetra-(4-methoxycarbonyl-phenoxy) nickel phthalocyanine (MeNiPc)

Me-CN_2 (0.56 g, 2 mmol) and dehydrated $(CH_3COO)_2Ni$ (0.15 g, 0.6 mmol) were added into 5 mL of dried 1-pentanol. After evacuating and purging with argon for three times, the reaction mixture was stirred at 115 °C until the reactants dissolved. Then, ~0.8 mL of DBU was quickly injected and continuously stirred at 135 °C for overnight. After the reaction finished and cooled, the dried crude product was purified by SiO_2 column chromatography using dichloromethane (CH_2Cl_2) as eluent to obtain a black solid with violet. Yield: 31.0%. FT-IR (KBr, υ, cm^{-1}): 2957, 2930, 2856, 1718, 1601, 1502, 1473, 1418, 1385, 1275, 1242, 1163, 1113, 1095, 1061, 1014, 959, 883, 748. Elem. Anal. Calcd. for $C_{64}H_{40}N_8O_{12}Ni$: C, 65.60; H, 3.44; N, 9.56. Found: C, 65.78; H, 3.49; N, 9.60. HRMS (m/z): Calcd. for $[M+Na]^+$: 1194.7614; Found: 1194.2316. UV-Vis (CH_2Cl_2, λ, nm): 329, 611, 672.

2.2.4. Synthesis of tetra-(4-tert-butylphenoxy) nickel phthalocyanine (TbNiPc)

The synthesis of TbNiPc was followed the procedure similar to that for MeNiPc. Specifically, Tb-CN_2 (0.55 g, 2 mmol), dehydrated $(CH_3COO)_2Ni$ (0.15 g, 0.6 mmol), dried 1-pentanol (5 mL) and DBU were employed to synthesize TbNiPc. Yield: 29.2%. FT-IR (KBr, υ, cm^{-1}): 2960, 2926, 2856, 1608, 1533, 1508, 1475, 1415, 1385, 1338, 1267, 1242, 1175, 1119, 1095, 1061, 1014, 959, 881, 818, 750. UV-Vis (CH_2Cl_2, λ, nm): 331, 622, 669.

2.2.5. Synthesis of 5,10,15,20-tetrakis(4-methoxycarbonylphenyl) porphyrin (MePp)

The compound MePp was synthesized following the reported method [40]. Methyl 4-formylbenzoate (5.0 g, 30 mmol) and redistilled pyrrole (2.2 g, 32 mmol) were hired in this synthesis. After dried, purple product was obtained with 56% yield. ^{1}H NMR based on CDCl₃, δ/ppm: 8.82 (d, 8 H, Aromatic ring-H), 8.46 (d, 8 H, Aromatic ring-H), 8.44 (d, 8 H, Aromatic ring-H), 4.11 (s, 12 H, -CH₃).

2.2.6. Synthesis of 5,10,15,20-tetrakis(4-tert-butylphenyl)porphyrin (TbPp)

The compound TbPp was synthesized according to the MePp. ^{1}H NMR based on CDCl₃, δ/ppm: 8.87 (d, 8 H, Aromatic ring-H), 8.16–8.14 (d, 8 H, Aromatic ring-H), 7.76–7.75 (d, 8 H, Aromatic ring-H), 1.61 (s, 36 H, -(CH₃)₃).

2.2.7. Synthesis of [5,10,15,20-tetrakis(4-methoxycarbonylphenyl) porphyrinato]-Ni(II) (MeNiPp)

The compound MeNiPp was synthesized according to the reported method [40]. FT-IR (KBr, υ, cm^{-1}): 2949, 1725, 1609, 1532, 1435, 1401, 1352, 1279, 1114, 1101, 1007, 1005, 824, 763. Elem. Anal. Calcd. for $C_{52}H_{36}N_4O_8Ni$: C, 69.12; H, 4.02; N, 6.20. Found: C, 69.32; H, 4.15; N, 6.31. HRMS (m/z): Calcd. for $[M]^+$: 902.1887; Found: 902.1825. UV-Vis (CH_2Cl_2, λ, nm): 414, 527.

2.2.8. Synthesis of [5,10,15,20-tetrakis(4-tert-butylphenyl)porphyrinato]-Ni(II) (TbNiPp)

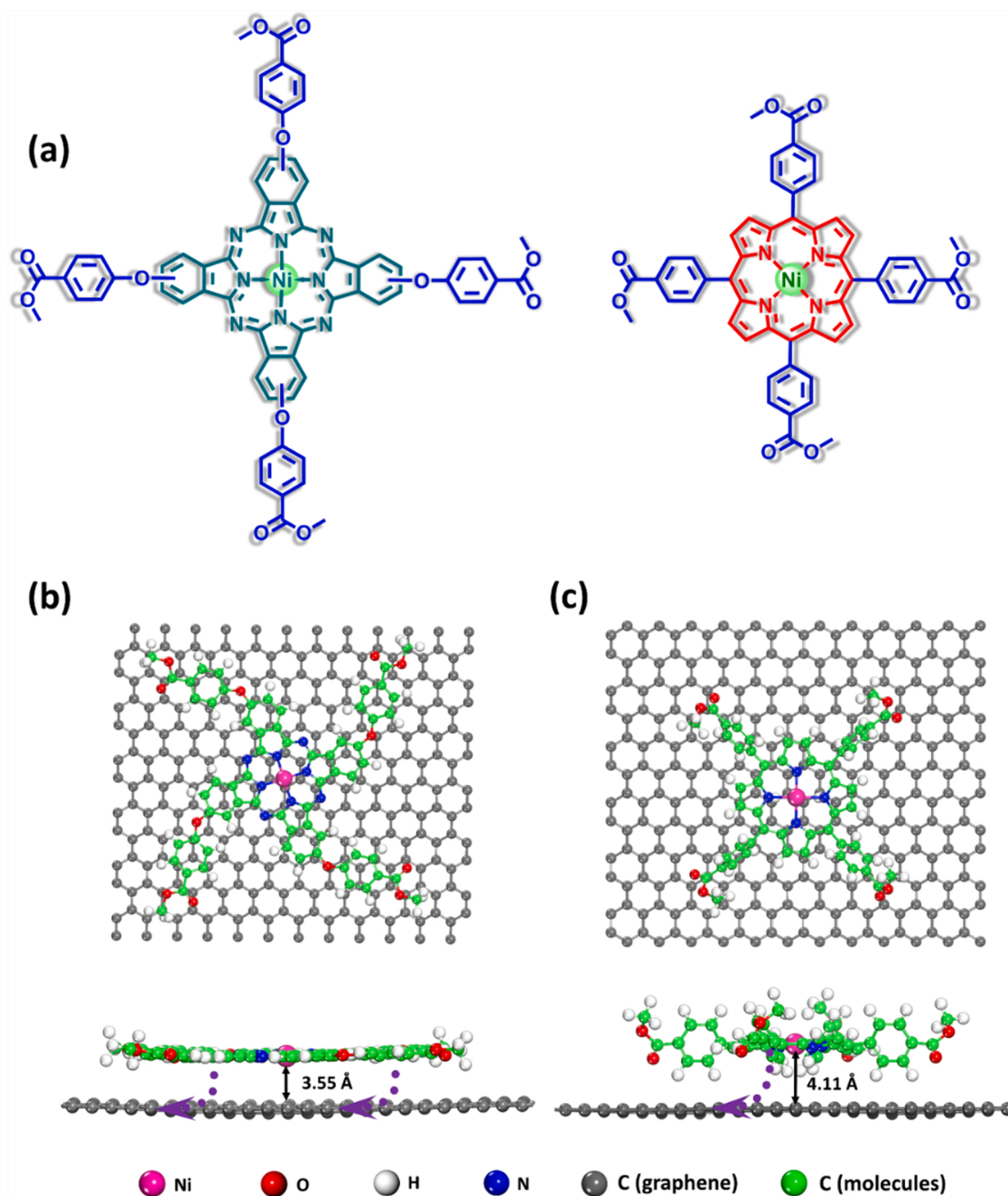The compound TbNiPp was synthesized by following the similar

Fig. 1. (a) Molecular structures of MeNiPc and MeNiPp, and top- and side-view images of DFT-optimized structures of (b) MeNiPc/G and (c) MeNiPp/G with the indicated heterointerfacial distances.

procedures to MeNiPp. FT-IR (KBr, υ, cm^{-1}): 2962, 2931, 2903, 2868,1508, 1460, 1385, 1352, 1267, 1111, 1072, 1007, 816, 791, 731, 714. UV-Vis (CH$_2$Cl$_2$, λ, nm): 414, 529.

2.2.9. Synthesis of MeCoPc and MeCoPp:

The control MeCoPc and MeCoPp were synthesized by following the similar procedures to MeNiPc and MeNiPp, respectively.

2.3. Preparation of catalysts

2.3.1. Preparation of MeNiPc/G

50 mg of graphene was dispersed in 10 mL of CH$_2$Cl$_2$ under ultrasound for 10 min, and then 10 mL of CH$_2$Cl$_2$ solution of MeNiPc (10.0 mg) was gradually added under stirring. After solvent evaporation, the catalyst was collected.

2.3.2. Preparation of TbNiPc/G, TbNiPp/G and MeNiPp/G

Following the same procedures, TbNiPc/G, TbNiPp/G and MeNiPp/G were prepared by controlling the addition amounts of TbNiPc (10.0
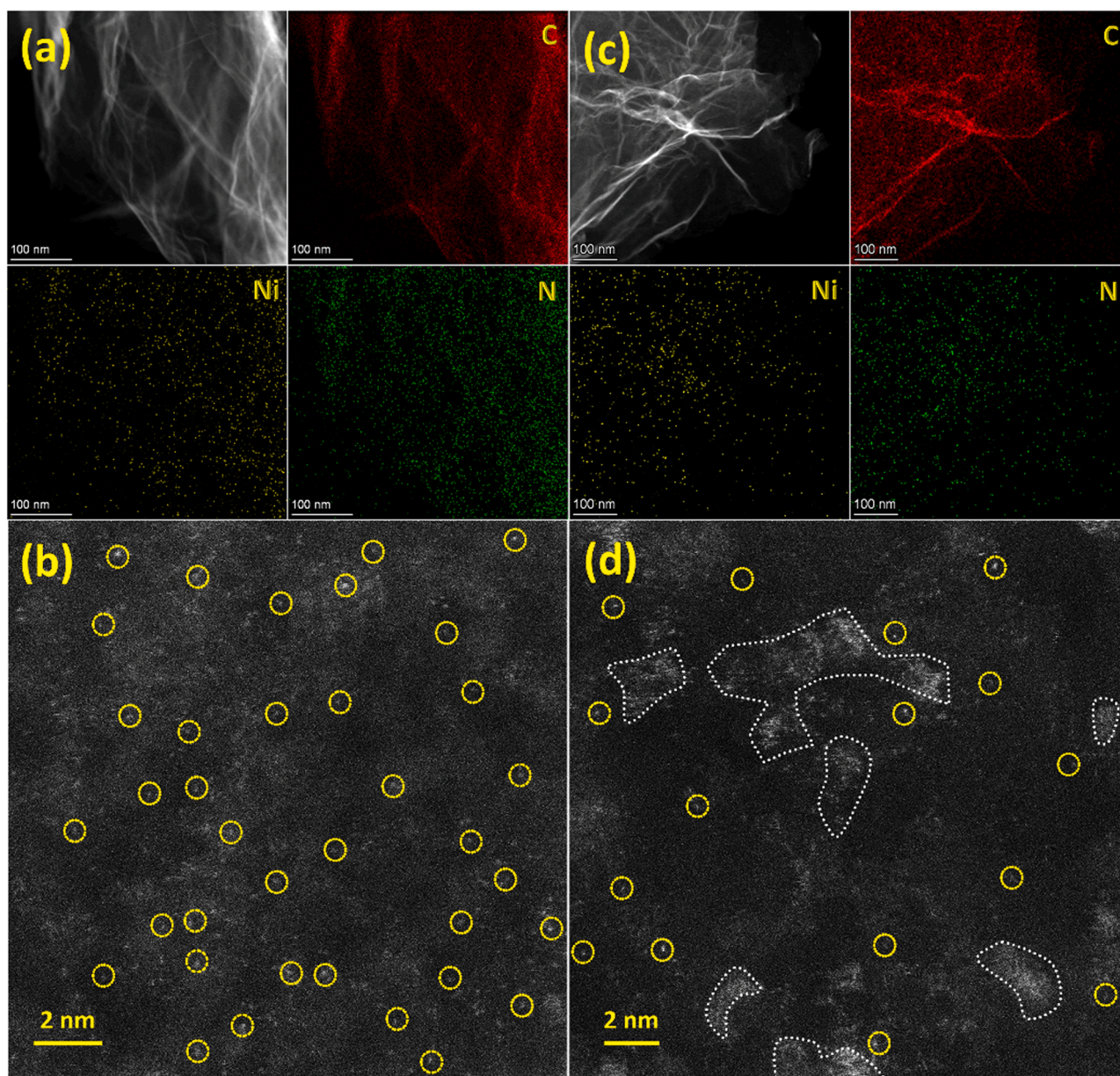
Fig. 2. The C, Ni and N of EDX elemental mappings and AC-HAADF-STEM images for MeNiPc/G (a, b) and MeNiPp/G (c, d).

mg), TbNiPp (7.4 mg) and MeNiPp (7.4 mg), respectively.

2.3.3. Preparation of MeNiPc/CB, MeNiPp/CB, MeCoPc/G, MeCoPp/G

Following the same procedures, MeNiPc/CB, MeNiPp/CB, MeCoPc/G, MeCoPp/G were prepared by above methods.

2.4. Preparation of working electrodes

Briefly, take MeNiPc/G as an example, 5.0 mg of MeNiPc/G sample was added into a centrifuge tube containing 0.7 mL of deionized H_2O, 0.2 mL of N,N-dimethylformamide and 0.1 mL of Nafion D-520 solution. After ultrasonicated for 60 min, the homogeneous seriflux was discretely drop-casted onto a carbon fibre paper (CFP) to form a homogeneous distribution with the area of 1 cm × 1 cm and the loading mass of ~0.5 mg cm^{-2}. And then, after air-dried for overnight, the working electrodes were used for testing.

2.5. Electrochemical measurements and computations

All the electrochemical measurements were performed according to our previous works [33,41]. Concretely, through bubbling pure CO_2 (99.999%) at a flow rate of 20 mL min^{-1}, CO_2-saturated 0.5 M $KHCO_3$ aqueous solution was hired as electrolyte in H-type cell test-system. The catalysts supported CFP, saturated Ag/AgCl electrode and Pt net (1 cm × 1 cm) were also engaged as the working electrode, the reference electrode and counter electrode, respectively. The gas products were detected by an online gas chromatograph (Agilent 7820 A), and liquid products were analyzed by quantitative NMR using DMSO as the internal standard.

The linear sweep voltammetry (LSV) polarization curves were obtained at the scan rate of 10.0 mV s^{-1}. I-t curve measurements were successively performed from − 0.58 to − 1.03 V vs. RHE at an interval of 0.05 V for 3600 s. The electrochemical impedance spectroscopies (EIS) were generated at potential − 0.58 V vs. RHE from 10^5 to 0.1 Hz. To obtain double-layer capacitance (C_{dl}), cyclic voltammograms (CV) were tested in the potential window of 0.02–0.12 V vs. RHE. All the potentials
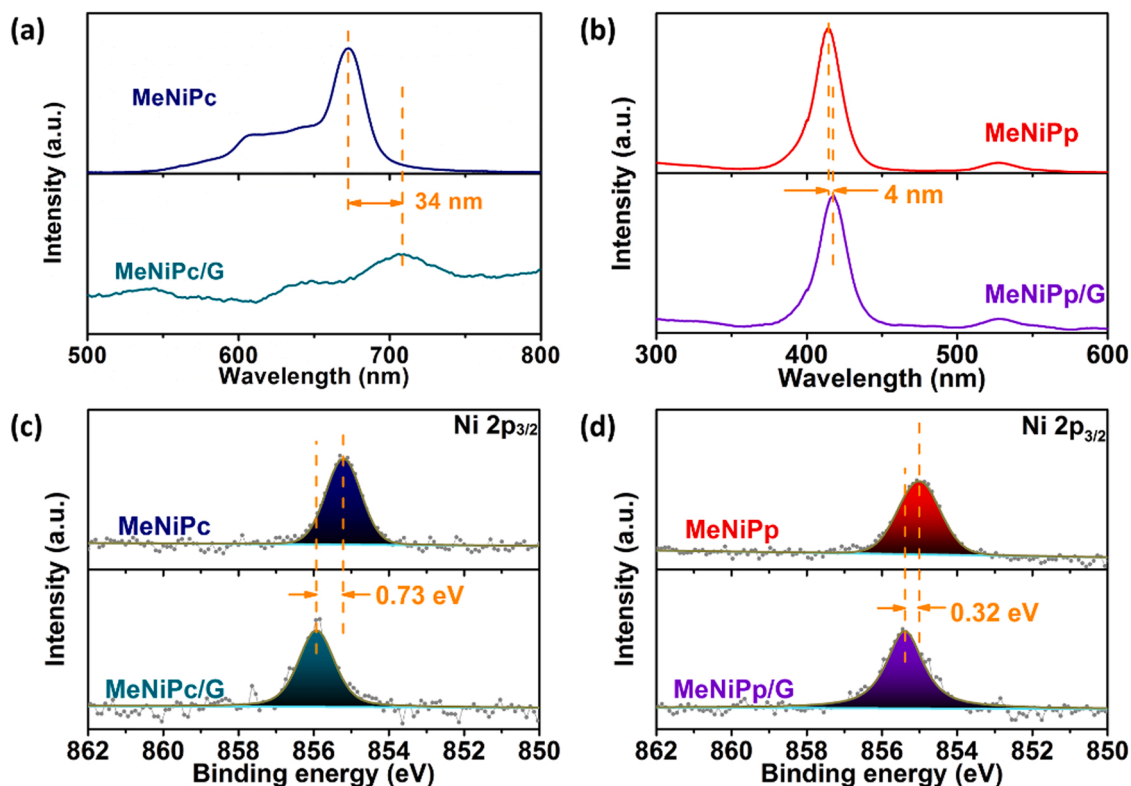
Fig. 3. UV-Vis spectra of MeNiPc and MeNiPc/G (a), MeNiPp and MeNiPp/G (b), Ni 2p$_{3/2}$ XPS spectra of MeNiPc and MeNiPc/G (c), MeNiPp and MeNiPp/G (d).

were converted based on the Nernst equation: E (vs. RHE) = E (vs. Ag/AgCl) + 0.1989 V + 0.059 × pH. All the potentials were without iR corrected.

In this work, density functional theory (DFT) calculations were carried out according to the method of our previous work [42]. Molecules were combined with a 12 × 12 × 1 zigzag type graphene. In addition, the gas-phase molecules were correspondingly treated as ideal gases [43].

2.6. Main characterizations

^{1}H NMR spectra of molecules and liquid products were carried out on an ECZ400S 400 MHz spectrometer. UV-Vis spectra of molecules and catalysts in liquid phase were collected at a Lambda 365 spectrophotometer. HR-MS were recorded from Agilent 6500 Series Q-TOF LC/MS system. The Ni loading amounts of the samples were detected from inductively coupled plasma atomic emission spectrometry (ICP-AES) on Ultima 2. The data of powder X-ray diffraction (PXRD) patterns were obtained on a benchtop X-ray diffractometer (Rigaku-Miniflex600) with a voltage of 40 kV and a current of 15 mA. Based on a Titan Cubed Themis G2 300 (FEI) high-resolution transmission electron microscope operated at 200 kV, aberration-corrected high angle annular dark-field scanning transmission electron microscopy (AC-HAADF-STEM) images were obtained. The images of scanning electron microscopy (SEM) was characterized on a ZEISS Sigma 300 field-emission scan electron microscope. The XPS data were recorded on a Thermo Fisher ESCALAB 250Xi spectrometer, using C 1 s (284.8 eV) as the reference line. For the Raman spectra, a Labram HR800 Renishaw inVia system (Horiba) was hired. The electrochemical measurements were performed on a CHI760E electrochemical workstation.

3. Results and discussion

3.1. Construction and characterization

As shown in Fig. 1a, tetra-(4-methoxycarbonyl-phenoxy) nickel phthalocyanine (MeNiPc) and 5,10,15,20-tetrakis(4-methoxycarbonyl-phenyl) nickel porphyrin (MeNiPp) were hired and their successful synthesis was confirmed (Figs.S1-S6). Their molecular structures are designed on the basis of rigorous Ni-N$_4$ active sites, distinguishable conjugate macrocycles and peripheral functional groups with similar electron-donating effects. Then, the MeNiPc/G composite was prepared by interacting MeNiPc with highly conductive graphene (G) in CH$_2$Cl$_2$ with the assistance of sonication and magnetic stirring. UV–Vis spectrum of the colorless transparent filtrate of MeNiPc/G indicates that the MeNiPc molecules were completely immobilized onto the graphene support (Fig.S7). For comparison, we also prepared MeNiPp/G with MeNiPp instead of MeNiPc under similar conditions. However, only partial MeNiPp was immobilized onto the graphene support, as demonstrated by the UV–Vis spectrum of red filtrate (Fig.S7). These phenomena reveal that MeNiPc can be easily anchored onto the sp^2 carbon of graphene via strong π-π interactions due to their planar and conjugated macrocyclic structures. By contrast, the four phenyls of MeNiPp are not coplanar with the central ring, which attenuates their π-π interactions with the graphene support [27,44,45]. Furthermore, to obtain more insight into the structure-induced heterointerfaces, DFT calculations were performed. As shown in Fig. 1b, a typical van der Waals distance of ~0.355 nm can be formed between MeNiPc and graphene, whereas the distance between MeNiPp and graphene is larger than the former sample, reaching to ~0.411 nm (Fig. 1c), which assuredly leads to the strength variation of the molecule-support interactions (including π-π and charge transfer interactions), providing a model platform to systematically comprehend the heterointerfacial effect of the heterogenized metallomacrocycles on the catalytic activity for electrochemical CO$_2$RR. In principle, the heterointerfacial effects induced by the varied strengths of molecular-support interactions will
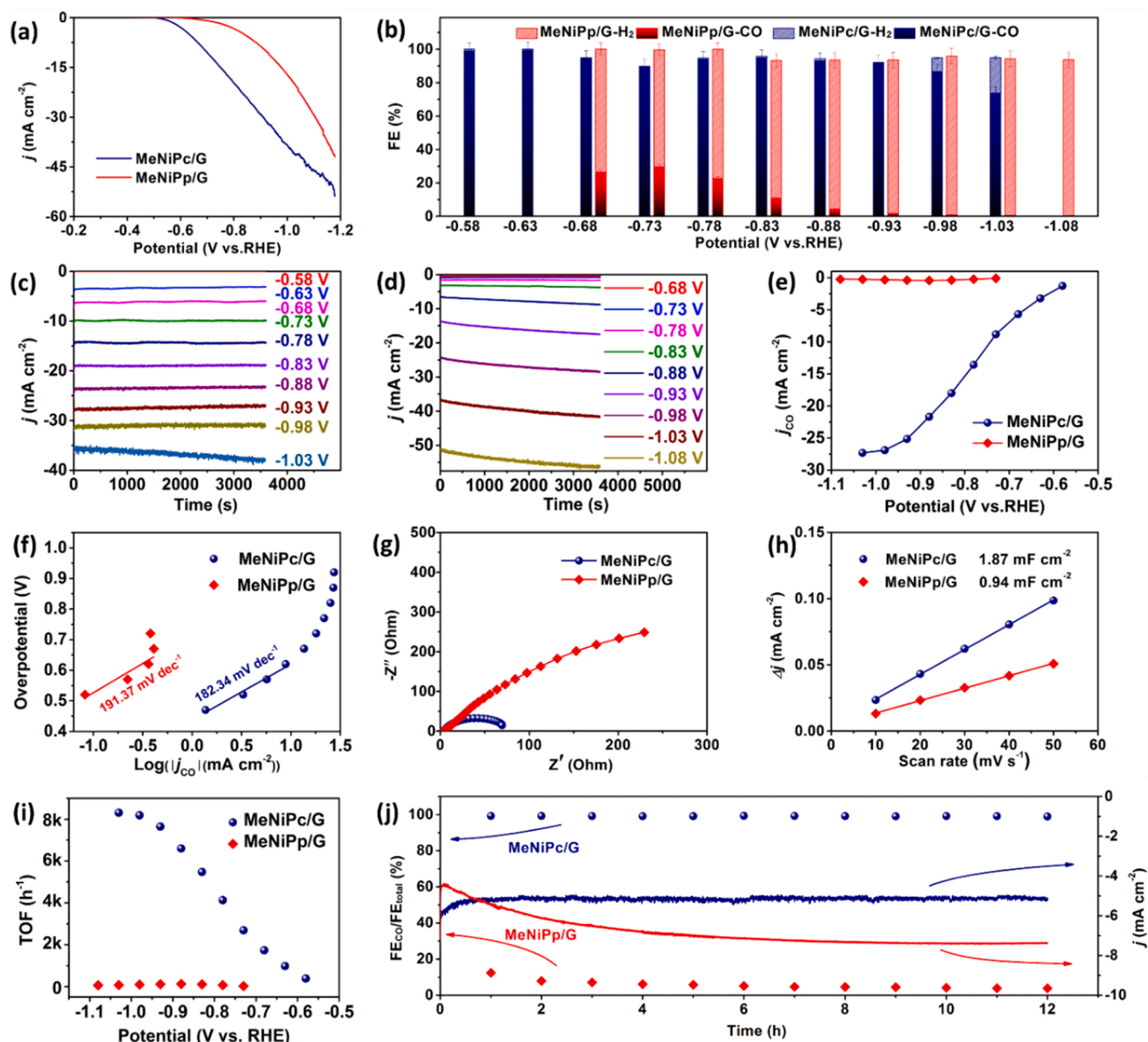
Fig. 4. CO$_2$RR performances of MeNiPc/G and MeNiPp/G: (a) LSVs, (b) FEs, (c, d) total current densities, (e) partial CO current densities, (f) Tafel slopes, (g) Nyquist plots, (h) capacitance values, (i) TOFs, and (j) stability test.

certainly regulate the electronic structures of the molecular active centers and thus the corresponding catalytic properties. To achieve the same loading, an impregnation method was further adopted to respectively prepare the MeNiPc/G and MeNiPp/G composites with the same mass fraction of Ni. Based on the ICP-AES, the content of Ni in MeNiPp/G was determined to be 0.76 wt%, which closes to that in MeNiPc/G (0.72 wt%) (Table S1). Notably, under the impregnation process, MeNiPc and MeNiPp can be solidified onto graphene upon solvent evaporation, but the contents are generally less than the theoretical values.

The SEM and TEM images of MeNiPc/G and MeNiPp/G were recorded in Fig.S8 and Fig.S9. The two-dimensional morphology of graphene was revealed in the large-scale range. Furthermore, according to the EDX elemental mappings, it is identified that the distributions of C, N and Ni elements in both MeNiPc/G and MeNiPp/G almost overlap and match well the graphene contours (Fig. 2a,c). Particularly, the homogeneous and coincident signals of Ni can be clearly found by the AC-HAADF-STEM (Fig. 2b), further verifying that the MeNiPc molecules are

uniformly immobilized on the graphene in MeNiPc/G. However, MeNiPp/G shows partial misdistribution due to the relatively weak heterointerfacial effect between MeNiPp and graphene (Fig. 2d). The PXRD, Raman spectroscopy, Brunauer-Emmett-Teller nitrogen sorption, and Fourier transform infrared spectroscopy (FT-IR) were further carried out to characterize MeNiPc/G and MeNiPp/G (Fig.S10). It should be pointed out that there is no palpable molecular aggregation in MeNiPc/G and MeNiPp/G, which faultlessly works in concert with the results of TEM. In addition to the visualization of AC-HAADF-STEM, to further gain more insight into the interaction of the MeNiPc/G and MeNiPp/G composites at the spectrum level, UV-Vis and XPS spectra were collected. As shown in the UV-Vis spectra (Fig. 3a), an evident red-shift of ~34 nm is observed for the Q-band of MeNiPc upon the immobilization on the graphene, indicating that the MeNiPc molecules are firmly immobilized on the graphene support with strong interactions. As to MeNiPp and MeNiPp/G, there is only a slight variation (~4 nm), revealing that the MeNiPp molecules are immobilized on graphene with much weaker interactions (Fig. 3b). Similarly, in the XPS spectrum of
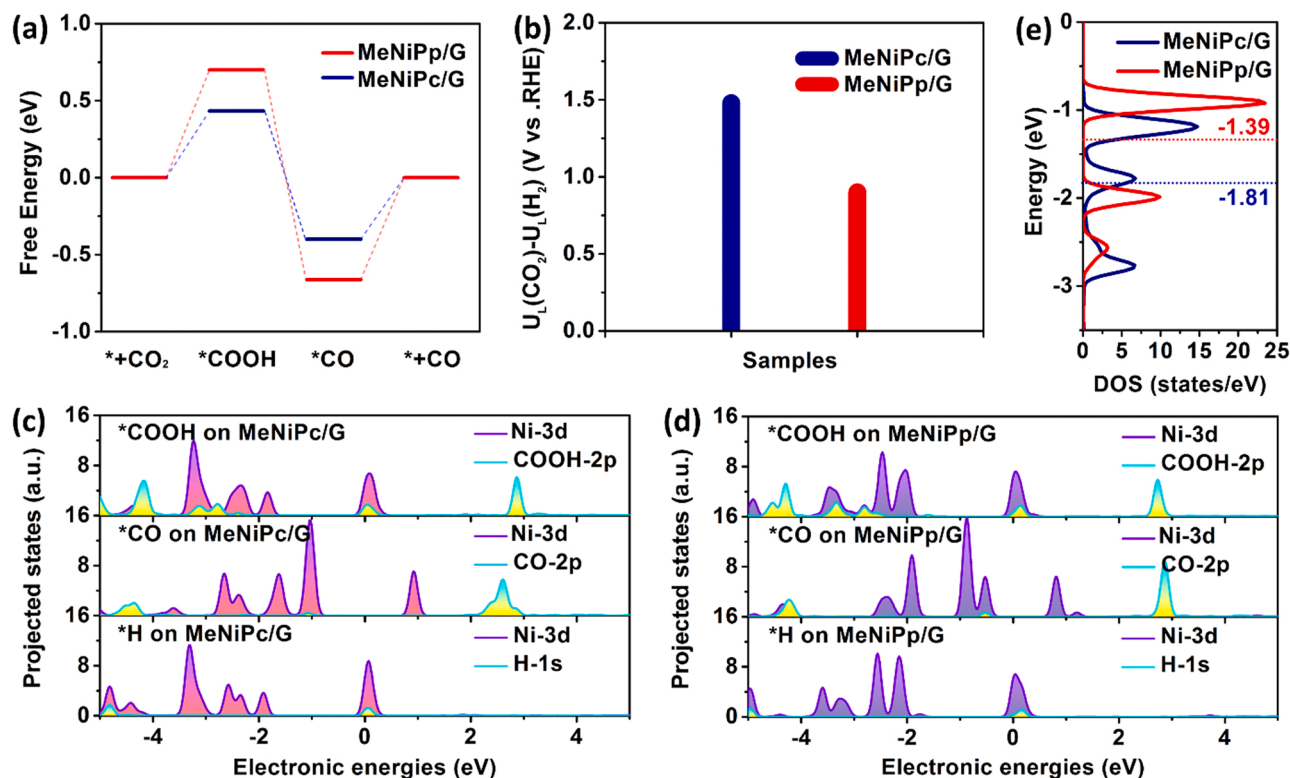
Fig. 5. (a) Calculated free energy diagrams for CO_2RR over MeNiPc/G and MeNiPp/G, (b) the differences in limiting potentials for CO_2RR ($U_L(CO_2)$) and HER ($U_L(H_2)$) over MeNiPc/G and MeNiPp/G, (c) PDOS of adsorption structures of *COOH, *CO, and *H on MeNiPc/G, (d) PDOS of adsorption structures of *COOH, *CO, and *H on MeNiPp/G, (e) projected DOS of Ni 3d in MeNiPc/G and MeNiPp/G.

MeNiPc/G (Fig. 3c), an obvious shift of ~0.73 eV to a higher binding energy was observed in the Ni $2p_{3/2}$ spectrum as compared to free MeNiPc, manifesting a distinct electron transfer from the coordinated Ni centers to the sp^2 carbon. Combining the single-molecular immobilization of MeNiPc on the graphene, such strong charge transfer interactions between the MeNiPc molecules and the carbon would further stabilize the heterojunction system and strengthen the heterointerfacial effect, which could be favorable to promote the intrinsic catalytic activity of the Ni-N$_4$ centers for CO_2RR. In comparison, the smaller shift between MeNiPp and MeNiPp/G (~0.32 eV) implies the weaker electron transfer and corresponding heterointerfacial effect in MeNiPp/G, due to the larger π-π distance (Fig. 3d).

3.2. Electrocatalytic performances for CO_2RR

To disclose the relationship between the heterointerfacial effect and the catalytic activity, the CO_2RR performances of MeNiPc/G and MeNiPp/G were studied in CO_2-saturated 0.5 M KHCO$_3$ solution with the same catalyst loading of 0.5 mg cm^{-2}. The yielded products were determined via gas chromatograph (GC) and nuclear magnetic resonance spectra (NMR), revealing the exclusive production of CO and H$_2$, without liquid products in the system (Fig. S11). As shown in Fig. 4a, the LSV curve of MeNiPc/G reveals the larger cathodic current densities and the positive shift of onset potential in the CO_2-saturated electrolyte compared to MeNiPp/G. Furthermore, combing with those in the Ar-saturated electrolytes (Fig.S12), the difference in the polarization curves clearly manifests that MeNiPc/G exhibits a much better electrocatalytic CO_2RR activity than that of MeNiPp/G [46]. In particular, the MeNiPc/G catalyst displays much greater current densities and FE$_{CO}$ than those of the MeNiPc and graphene individuals, demonstrating that the synergistic heterointerfacial effect between MeNiPc and graphene remarkably improves the intrinsic catalytic performance of the MeNiPc molecules (Figs.S13-S15). It should be noted that MeNiPc/G shows the

greatly larger FE$_{CO}$ in a wide potential range compared with MeNiPp/G (Fig. 4b), indicating the dominant CO_2RR and hydrogen evolution reaction (HER) over MeNiPc/G and MeNiPp/G, respectively, under the same catalytic conditions. The catalytic performance of MeNiPc/G is also comparable to the previous excellent results that have been reported under KHCO$_3$ environments (Table S2). Meanwhile, the CO partial current densities (j_{CO}) of MeNiPc/G at working potentials are 1–2 orders of magnitude larger than those of MeNiPp/G (Figs. 4c-4e). In addition, as shown in Fig. 4f, the Tafel slope of MeNiPc/G fitted with the current densities of CO and overpotentials was assessed to be 182.34 mV dec^{-1}, which is smaller than that of MeNiPp/G (191.37 mV dec^{-1}), clarifying the improved reaction kinetics and electron transfer of MeNiPc/G for CO_2RR compared to MeNiPp/G. These results are consistent with the electrochemical impedance spectroscopy (EIS) characterization as shown in Fig. 4g, indicating that MeNiPc/G has the lower interfacial charge transfer resistance. The electrochemical active surface areas (ECSA) of MeNiPc/G and MeNiPp/G were further estimated by measuring the double-layer capacitance (Fig.S16 and Fig. 4h). Accordingly, the ECSA of MeNiPc/G was estimated to be twice higher than that of MeNiPp/G, reflecting that there are more effective active sites in MeNiPc/G due to the strong heterointerfacial effect with the optimized distance. The turn of frequency (TOF) for a catalytic reaction is important to evaluate the intrinsic catalytic ability of the electrocatalyst. As seen in Fig. 4i, the TOF value of the MeNiPc/G catalyst was calculated to be 2687 and 8310 h^{-1} at − 0.73 and − 1.03 V vs. RHE, respectively, which are ~113 and ~117 times those of the MeNiPp/G catalyst. Moreover, Fig. 4j shows that the achieved current density and FE$_{CO}$ of the MeNiPc/G catalyst have no obvious change at − 0.68 V vs. RHE during the 12-hour stability test. However, much inferior stability as well as poor selectivity was observed for MeNiPp/G. After the durability tests, the operated electrocatalysts were further surveyed by UV-Vis spectroscopy and PXRD (Fig.S17 and Fig.S18). Notably, the characteristic absorption peaks of MeNiPc on graphene showed no
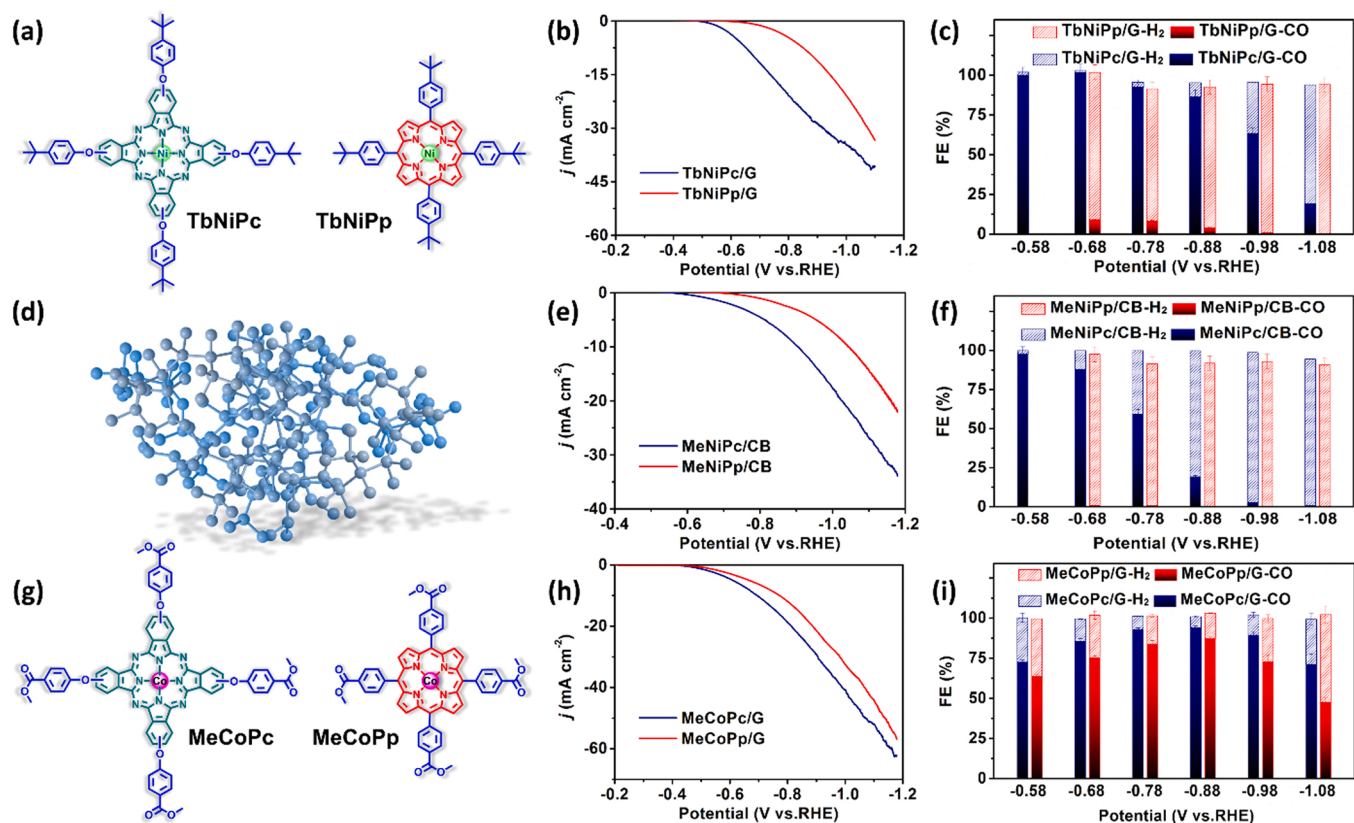
Fig. 6. (a) Molecular structures of TbNiPc and TbNiPp, (b) LSV curves and (c) FEs of TbNiPc/G and TbNiPp/G, (d) 3D model of carbon black (CB) with sp^3 hybridization, (e) LSV curves and (f) FEs of MeNiPc/CB and MeNiPp/CB, (g) molecular structures of MeCoPc and MeCoPp, (h) LSV curves and (i) FEs of MeCoPc/G and MeCoPp/G.

obvious change, while that of MeNiPp on graphene was not remained at the initial level. Consequently, the above results suggest that MeNiPc/G with stronger heterointerfacial effect exhibits the better catalytic performance of CO_2RR toward CO compared with MeNiPp/G, which was also verified by the DFT forecast and structure characteristics.

3.3. DFT calculations

DFT calculations were carried out to further investigate the effect of the heterointerfacial structure differences between MeNiPc/G and MeNiPp/G on CO_2RR. The Gibbs free energy diagrams for each reaction step of CO_2RR process over MeNiPc/G and MeNiPp/G are illustrated in Fig. 5a. Obviously, the formation of *COOH intermediate over MeNiPc/G is closer to 0 eV compared to MeNiPp/G, indicating that the Ni sites in MeNiPc/G have high activity for CO_2-to-CO. Moreover, unlike the favorable CO desorption on MeNiPc/G, the strong binding energy of *CO on the Ni sites of MeNiPp/G limits the desorption of CO, thus limiting its the catalytic performance [47]. As illustrated in Fig. 5b, the differences between the thermodynamic limiting potentials for the processes of CO_2RR and HER over MeNiPc/G and MeNiPp/G were further compared, as the more positive value suggests the higher selectivity toward CO_2RR. As expected, MeNiPc/G shows a higher limiting potential difference value of 1.53 V, indicating that MeNiPc/G is capable of delivering the higher selectivity for CO_2RR [48], in good agreement with the experimental results. Moreover, the differences in adsorption energies on MeNiPc/G and MeNiPp/G for CO_2RR are further understood via the electronic structure calculations. As shown in Fig. 5c, d, upon the adsorption of *COOH, *CO, and *H, the 3d orbitals of the Ni centers in MeNiPc/G and MeNiPp/G have analogous projected states [49]. In particular, in comparison to MeNiPp/G, when the Ni site of MeNiPc bonds with *CO, the 3d orbital of Ni is delocalized toward the lower

energy region on the surface of MeNiPc/G, which could facilitate the desorption of *CO and enhance the catalytic performance [50]. In addition, as can be seen from Fig. 5e, compared with MeNiPc/G, the d-band center of the Ni site in MeNiPp/G is closer to the Fermi level, indicating the stronger bonding with *CO that will lead to the poisoning of the active centers in MeNiPp/G [48,51], which is corresponding to the experimental result shown in Fig. 4j.

3.4. Universality of heterointerface engineering

In order to further evaluate the universality of the heterointerface engineering in the heterogenized metallomacrocycles for CO_2RR, we systematically investigated from the following aspects: functional groups, supports and central metals. As depicted in Fig. 6a, tetra-(4-tert-butylphenoxy) nickel phthalocyanine (TbNiPc) and 5,10,15,20-tetrakis (4-tert-butylphenyl) nickel porphyrin (TbNiPp) were further hired to immobilize on the graphene for CO_2-to-CO conversion. Compared with the TbNiPp/G composite, TbNiPc/G exhibits the better CO_2RR performance, in terms of onset potential, current density and FE_{CO} (Figs. 6b, 6c, S19), displaying the same tendency observed for MeNiPc/G and MeNiPp/G. In particular, the FE_{CO} of TbNiPp/G at different potentials are about half those of MeNiPp/G, suggesting that the heterointerfacial effect of TbNiPp/G is further weakened due to the spatial elongation of tert-butyl groups. These results indicate that the heterointerface effect of catalysts for CO_2RR not only originates from the conjugate macrocycles but also is influenced by the peripheral functional groups, and the immobilization of the non-rigid group modified nickel phthalocyanines (e.g., MeNiPc and TbNiPc) to graphene would result in a superior heterointerface effect in favor of CO_2RR. On the other hand, the role of supports cannot be ignored in CO_2RR. Different from the graphene with perfect flat sp^2 carbon domains, carbon black (CB) features a non-layer

microstructure with abundant sp^3 carbon fractions (Fig. 6d) [52–54], which is pernicious to the construction of the favorable heterointerface for modulating the interactions between the metallomacrocycle molecules and the substrates. As expected, the current densities and FE$_{CO}$ of MeNiPc/CB and MeNiPp/CB are much lower than those of MeNiPc/G and MeNiPp/G at the same potentials (Figs. 6e, 6f, S20), due to the difference in their heterointerfacial effect. Moreover, compared with the graphene-immobilized catalysts, the stability of the CB-based counterparts is much inferior owing to the weaker interactions and gradual H$_2$ formation. Furthermore, the Co-based macrocyclic molecules (MeCoPc and MeCoPp) were also developed as shown in Fig. 6g. Similarly, the corresponding MeCoPc/G with the more propitious heterointerface structure exhibits the higher current densities and FE$_{CO}$ for electrochemical CO$_2$-to-CO conversion, further highlighting the superiority of the optimized heterointerfacial effect and the universality of the heterointerface engineering for improving the catalytic performances in the metallomacrocycle-based catalysts (Figs. 6h, 6i, S21) [38,55–57].

4 Conclusions

In summary, we have theoretically and experimetally deciphered the significant influences of heterointerfacial effect on catalytic performances via constructing the graphene-immobilized well-structured nickel phthalocyanine and porphyrin macrocycles and comparing their electrocatalytic performances for CO$_2$ reduction. Owing to their different steric hindrance in the immobilized metallomacrocycle molecules, the heterointerfacial effects that are induced by the varied strengths of the molecule-support interactions including π-π and charge transfer interactions modulate the electronic structures of the metal centers and thus the intrinsic catalytic properties. Veritably, the MeNiPc/G composite with optimized heterointerfacial effect exhibits much superior catalytic performance with high FE$_{CO}$ of ~99% and large current densities in a wide potential window, tens of times that of the MeNiPp/G counterpart. Additionally, systematic research on the metallomacrocycle-based catalysts with different functional groups, supports and central metals revealed that the heterointerfacial effect is ubiquitous and plays a crucial role in electrocatalysis. These findings will advance the design and construction of efficient metallomacrocycle-based catalysts with optimized heterointerface for CO$_2$RR and other electrochemical synthesis.

CRediT authorship contribution statement

Meng-Ke Hu: Investigation, Methodology, Formal analysis, Validation, Writing – original draft. **Sheng-Hua Zhou:** Formal analysis, Writing – review & editing. **Dong-Dong Ma:** Conceptualization, Formal analysis, Visualization, Validation, Writing – original draft. **Qi-Long Zhu:** Supervision, Conceptualization, Data curation, Writing – review & editing.

Declaration of Competing Interest

The authors declare that they have no known competing financial interests or personal relationships that could have appeared to influence the work reported in this paper.

Acknowledgements

Appendix A. Supporting information

Supplementary data associated with this article can be found in the online version at doi:10.1016/j.apcatb.2022.121324.

References

[1] Y. Wu, Z. Jiang, X. Lu, Y. Liang, H. Wang, Domino electroreduction of CO$_2$ to methanol on a molecular catalyst, Nature 575 (2019) 639–642, https://doi.org/10.1038/s41586-019-1760-8.

[2] C.T. Dinh, T. Burdyny, M.G. Kibria, A. Seifitokaldani, C.M. Gabardo, F.P.G. de Arquer, A. Kiani, J.P. Edwards, P. De Luna, O.S. Bushuyev, C.Q. Zou, R. Quintero-Bermudez, Y.J. Pang, D. Sinton, E.H. Sargent, CO$_2$ electroreduction to ethylene via hydroxide-mediated copper catalysis at an abrupt interface, Science 360 (2018) 783–787, https://doi.org/10.1126/science.aas9100.

[3] X. Li, Q.-L. Zhu, MOF-based materials for photo- and electrocatalytic CO$_2$ reduction, EnergyChem 2 (2020), 100033, https://doi.org/10.1016/j.enchem.2020.100033.

[4] H.-J. Zhu, M. Lu, Y.-R. Wang, S.-J. Yao, M. Zhang, Y.-H. Kan, J. Liu, Y. Chen, S.-L. Li, Y.-Q. Lan, Efficient electron transmission in covalent organic framework nanosheets for highly active electrocatalytic carbon dioxide reduction, Nat. Commun. 11 (2020) 497, https://doi.org/10.1038/s41467-019-14237-4.

[5] S.G. Han, D.-D. Ma, Q.L. Zhu, Atomically structural regulations of carbon-based single-atom catalysts for electrochemical CO$_2$ reduction, Small Methods 5 (2021), 2100102, https://doi.org/10.1002/smtd.202100102.

[6] C. Cao, D.-D. Ma, J. Jia, Q. Xu, X.T. Wu, Q.L. Zhu, Divergent paths, same goal: a pair-electrosynthesis tactic for cost-efficient and exclusive formate production by metal-organic-framework-derived 2D electrocatalysts, Adv. Mater. 33 (2021), 2008631, https://doi.org/10.1002/adma.202008631.

[7] C. Yang, Z. Gao, D. Wang, S. Li, J. Li, Y. Zhu, H. Wang, W. Yang, X.J. Gao, Z. Zhang, W. Hu, Bimetallic phthalocyanine heterostructure used for highly selective electrocatalytic CO$_2$ reduction, Sci. China Mater. (2021), https://doi.org/10.1007/s40843-021-1749-5.

[8] S. Wei, H. Zou, W. Rong, F. Zhang, Y. Ji, L. Duan, Conjugated nickel phthalocyanine polymer selectively catalyzes CO$_2$-to-CO conversion in a wide operating potential window, Appl. Catal. B- Environ. 284 (2021), 119739, https://doi.org/10.1016/j.apcatb.2020.119739.

[9] Y. Zhao, X.L. Liu, D.C. Chen, Z.X. Liu, Q.C. Yang, X. Lin, M. Peng, P. Liu, Y.W. Tan, Atomic-level-designed copper atoms on hierarchically porous gold architectures for high-efficiency electrochemical CO$_2$ reduction, Sci. China Mater. 64 (2021) 1900–1909, https://doi.org/10.1007/s40843-020-1583-4.

[10] J.G. Wang, S.L. Ning, M. Luo, D. Xiang, W. Chen, X.W. Kang, Z. Jiang, S.W. Chen, In-Sn alloy core-shell nanoparticles: In-doped SnO$_x$ shell enables high stability and activity towards selective formate production from electrochemical reduction of CO$_2$, Appl. Catal. B- Environ. 288 (2021), 119979, https://doi.org/10.1016/j.apcatb.2021.119979.

[11] D. Chen, Q.F. Yao, P.L. Cui, H. Liu, J.P. Xie, J. Yang, Tailoring the selectivity of bimetallic copper-palladium nanoalloys for electrocatalytic reduction of CO$_2$ to CO, ACS Appl. Energy Mater. 1 (2018) 883–890, https://doi.org/10.1021/acsaem.7b00320.

[12] S.X. Ren, D. Joulie, D. Salvatore, K. Torbensen, M. Wang, M. Robert, C.P. Berlinguette, Molecular electrocatalysts can mediate fast, selective CO$_2$ reduction in a flow cell, Science 365 (2019) 367–369, https://doi.org/10.1126/science.aax4608.

[13] Y.S. Wu, Y.Y. Liang, H.L. Wang, Heterogeneous molecular catalysts of metal phthalocyanines for electrochemical CO$_2$ reduction reactions, Acc. Chem. Res. 54 (2021) 3149–3159, https://doi.org/10.1021/acs.accounts.1c00200.

[14] X.Y. Liu, B.Q. Li, B. Ni, L. Wang, H.J. Peng, A perspective on the electrocatalytic conversion of carbon dioxide to methanol with metallomacrocyclic catalysts, J. Energy Chem. 64 (2022) 263–275, https://doi.org/10.1016/j.jechem.2021.04.059.

[15] K. Guo, H. Lei, X. Li, Z. Zhang, Y. Wang, H. Guo, W. Zhang, R. Cao, Alkali metal cation effects on electrocatalytic CO$_2$ reduction with iron porphyrins, Chin. J. Catal. 42 (2021) 1439–1444, https://doi.org/10.1016/S1872-2067(20)63762-7.

[16] B. Zhao, H. Lei, N. Wang, G. Xu, W. Zhang, R. Cao, Underevaluated solvent effects in the electrocatalytic CO$_2$ reduction by Fe^{III} chloride tetrakis(pentafluorophenyl) porphyrin, Chem. Eur. J. 26 (2020) 4007–4012, https://doi.org/10.1002/chem.201903064.

[17] Z.Z. Liang, H.Y. Wang, H.Q. Zheng, W. Zhang, R. Cao, Porphyrin-based frameworks for oxygen electrocatalysis and catalytic reduction of carbon dioxide, Chem. Soc. Rev. 50 (2021) 2540–2581, https://doi.org/10.1039/d0cs01482f.

[18] B. Han, Y. Jin, B. Chen, W. Zhou, B. Yu, C. Wei, H. Wang, K. Wang, Y. Chen, B. Chen, J. Jiang, Maximizing electroactive sites in a three-dimensional covalent organic framework for significantly improved carbon dioxide reduction electrocatalysis, Angew. Chem. Int. Ed. 61 (2022), e202114244, https://doi.org/10.1002/anie.202114244.

[19] Y.Z. Liu, S. Li, L. Dai, J.N. Li, J.N. Lv, Z.J.J. Zhu, A.X. Yin, P.F. Li, B. Wang, The synthesis of hexaazatrinaphthylene-based 2D conjugated copper metal-organic framework for highly selective and stable electroreduction of CO$_2$ to methane, Angew. Chem. Int. Ed. 60 (2021) 16409–16415, https://doi.org/10.1002/anie.202105966.

[20] N. Corbin, J. Zeng, K. Williams, K. Manthiram, Heterogeneous molecular catalysts for electrocatalytic CO$_2$ reduction, Nano Res. 12 (2019) 2093–2125, https://doi.org/10.1007/s12274-019-2403-y.

[21] F.W. Li, A. Thevenon, A. Rosas-Hernandez, Z.Y. Wang, Y.L. Li, C.M. Gabardo, A. Ozden, C.T. Dinh, J. Li, Y.H. Wang, J.P. Edwards, Y. Xu, C. McCallum, L.Z. Tao, Z.Q. Liang, M.C. Luo, X. Wang, H.H. Li, C.P. O'Brien, C.S. Tan, D.H. Nam, R. Quintero-Bermudez, T.T. Zhuang, Y.G.C. Li, Z.J. Han, R.D. Britt, D. Sinton, T. Agapie, J.C. Peters, E.H. Sargent, Molecular tuning of CO$_2$-to-ethylene conversion, Nature 577 (2020) 509–513, https://doi.org/10.1038/s41586-019-1782-2.

[22] C. Costentin, S. Drouet, M. Robert, J.M. Saveant, A local proton source enhances CO$_2$ electroreduction to CO by a molecular Fe catalyst, Science 338 (2012) 90–94, https://doi.org/10.1126/science.1224581.

[23] S. Lin, C.S. Diercks, Y.B. Zhang, N. Kornienko, E.M. Nichols, Y.B. Zhao, A.R. Paris, D. Kim, P. Yang, O.M. Yaghi, C.J. Chang, Covalent organic frameworks comprising cobalt porphyrins for catalytic CO$_2$ reduction in water, Science 349 (2015) 1208–1213, https://doi.org/10.1126/science.aac8343.

[24] X. Zhang, Z.S. Wu, X. Zhang, L.W. Li, Y.Y. Li, H.M. Xu, X.X. Li, X.L. Yu, Z.S. Zhang, Y.Y. Liang, H.L. Wang, Highly selective and active CO$_2$ reduction electro-catalysts based on cobalt phthalocyanine/carbon nanotube hybrid structures, Nat. Commun. 8 (2017) 14675, https://doi.org/10.1038/ncomms14675.

[25] F. Franco, C. Rettenmaier, H.S. Jeon, B. Roldan Cuenya, Transition metal-based catalysts for the electrochemical CO$_2$ reduction: from atoms and molecules to nanostructured materials, Chem. Soc. Rev. 49 (2020) 6884–6946, https://doi.org/10.1039/d0cs00835d.

[26] J. Wang, X. Huang, S. Xi, H. Xu, X. Wang, Axial modification of cobalt complexes on heterogeneous surface with enhanced electron transfer for carbon dioxide reduction, Angew. Chem. Int. Ed. 59 (2020) 19162–19167, https://doi.org/10.1002/anie.202008759.

[27] B. Hu, W. Xie, R. Li, Z. Pan, S. Song, Y. Wang, How does the ligands structure surrounding metal-N$_4$ of Co-based macrocyclic compounds affect electrochemical reduction of CO$_2$ performance, Electrochim. Acta 331 (2020), 135283, https://doi.org/10.1016/j.electacta.2019.135283.

[28] N. Leonard, W. Ju, I. Sinev, J. Steinberg, F. Luo, A.S. Varela, B. Roldan Cuenya, P. Strasser, The chemical identity, state and structure of catalytically active centers during the electrochemical CO$_2$ reduction on porous Fe-nitrogen-carbon (Fe-N-C) materials, Chem. Sci. 9 (2018) 5064–5073, https://doi.org/10.1039/c8sc00491a.

[29] A.S. Varela, W. Ju, P. Strasser, Molecular Nitrogen-Carbon Catalysts, Molecular nitrogen-carbon catalysts, solid metal organic framework catalysts, and solid metal/nitrogen-doped carbon (MNC) catalysts for the electrochemical CO$_2$ reduction, Adv. Energy Mater. 8 (2018), 1703614, https://doi.org/10.1002/aenm.201703614.

[30] J. Wang, X. Huang, S. Xi, J.-M. Lee, C. Wang, Y. Du, X. Wang, Linkage effect in the heterogenization of cobalt complexes by doped graphene for electrocatalytic CO$_2$ reduction, Angew. Chem. Int. Ed. 58 (2019) 13532–13539, https://doi.org/10.1002/anie.201906475.

[31] S. Dou, L. Sun, S. Xi, X. Li, T. Su, H.J. Fan, X. Wang, Enlarging the π-conjugation of cobalt porphyrin for highly active and selective CO$_2$ electroreduction, ChemSusChem 14 (2021) 2126–2132, https://doi.org/10.1002/cssc.202100176.

[32] X. Zhang, Y. Wang, M. Gu, M. Wang, Z. Zhang, W. Pan, Z. Jiang, H. Zheng, M. Lucero, H. Wang, G.E. Sterbinsky, Q. Ma, Y.-G. Wang, Z. Feng, J. Li, H. Dai, Y. Liang, Molecular engineering of dispersed nickel phthalocyanines on carbon nanotubes for selective CO$_2$ reduction, Nat. Energy 5 (2020) 684–692, https://doi.org/10.1038/s41560-020-0667-9.

[33] D.-D. Ma, S.-G. Han, C. Cao, X. Li, X.-T. Wu, Q.-L. Zhu, Remarkable electrocatalytic CO$_2$ reduction with ultrahigh CO/H$_2$ ratio over single-molecularly immobilized pyrrolidinonyl nickel phthalocyanine, Appl. Catal. B-Environ. 264 (2020) 118530, https://doi.org/10.1016/j.apcatb.2019.118530.

[34] J. Su, J.-J. Zhang, J. Chen, Y. Song, L. Huang, M. Zhu, B.I. Yakobson, B.Z. Tang, R. Ye, Building a stable cationic molecule/electrode interface for highly efficient and durable CO$_2$ reduction at an industrially relevant current, Energy Environ. Sci. 14 (2021) 483–492, https://doi.org/10.1039/d0ee02535f.

[35] D.-D. Ma, S.-G. Han, C. Cao, W. Wei, X. Li, B. Chen, X.-T. Wu, Q.-L. Zhu, Bifunctional single-molecular heterojunction enables completely selective CO$_2$-to-CO conversion integrated with oxidative 3D nano-polymerization, Energy Environ. Sci. 14 (2021) 1544–1552, https://doi.org/10.1039/d0ee03731a.

[36] X. Ren, S. Liu, H. Li, J. Ding, L. Liu, Z. Kuang, L. Li, H. Yang, F. Bai, Y. Huang, T. Zhang, B. Liu, Electron-withdrawing functional ligand promotes CO$_2$ reduction catalysis in single atom catalyst, Sci. China Chem. 63 (2020) 1727–1733, https://doi.org/10.1007/s11426-020-9847-9.

[37] L. Sun, Z. Huang, V. Reddu, T. Su, A.C. Fisher, X. Wang, A planar, conjugated N$_4$-macrocyclic cobalt complex for heterogeneous electrocatalytic CO$_2$ reduction with high activity, Angew. Chem. Int. Ed. 59 (2020) 17104–17109, https://doi.org/10.1002/anie.202007445.

[38] Y. Wang, X.-P. Zhang, H. Lei, K. Guo, G. Xu, L. Xie, X. Li, W. Zhang, U.-P. Apfel, R. Cao, Tuning electronic structures of covalent Co porphyrin polymers for electrocatalytic CO$_2$ reduction in aqueous solutions, CCS Chem. 4 (2022), https://doi.org/10.31635/ccschem.022.202101706.

[39] K. Chen, M. Cao, Y. Lin, J. Fu, H. Liao, Y. Zhou, H. Li, X. Qiu, J. Hu, X. Zheng, M. Shakouri, Q. Xiao, Y. Hu, J. Li, J. Liu, E. Cortés, M. Liu, Ligand engineering in nickel phthalocyanine to boost the electrocatalytic reduction of CO$_2$, Adv. Funct. Mater. 31 (2021), 2111322, https://doi.org/10.1002/adfm.202111322.

[40] D.W. Feng, W.C. Chung, Z.W. Wei, Z.Y. Gu, H.L. Jiang, Y.P. Chen, D. J. Darensbourg, H.C. Zhou, Construction of ultrastable porphyrin Zr metal-organic frameworks through linker elimination, J. Am. Chem. Soc. 135 (2013) 17105–17110, https://doi.org/10.1021/ja408084j.

[41] X. Chen, D.-D. Ma, B. Chen, K. Zhang, R. Zou, X.-T. Wu, Q.-L. Zhu, Metal-organic framework-derived mesoporous carbon nanoframes embedded with atomically dispersed Fe-N active sites for efficient bifunctional oxygen and carbon dioxide electroreduction, Appl. Catal. B Environ. 267 (2020), 118720, https://doi.org/10.1016/j.apcatb.2020.118720.

[42] S.-G. Han, D.-D. Ma, S.-H. Zhou, K. Zhang, W.-B. Wei, Y. Du, X.-T. Wu, Q. Xu, R. Zou, Q.-L. Zhu, Fluorine-tuned single-atom catalysts with dense surface Ni-N$_4$ sites on ultrathin carbon nanosheets for efficient CO$_2$ electroreduction, Appl. Catal. B-Environ. 283 (2021), 119591, https://doi.org/10.1016/j.apcatb.2020.119591.

[43] A.A. Peterson, F. Abild-Pedersen, F. Studt, J. Rossmeisl, J.K. Norskov, How copper catalyzes the electroreduction of carbon dioxide into hydrocarbon fuels, Energy Environ. Sci. 3 (9) (2010) 1311–1315, https://doi.org/10.1039/C0EE00071J.

[44] X.M. Hu, M.H. Ronne, S.U. Pedersen, T. Skrydstrup, K. Daasbjerg, Enhanced catalytic activity of cobalt porphyrin in CO$_2$ electroreduction upon immobilization on carbon materials, Angew. Chem. Int. Ed. 56 (2017) 6468–6472, https://doi.org/10.1002/anie.201701104.

[45] J.-H. Wang, Y. Zhang, M. Liu, G.-K. Gao, W. Ji, C. Jiang, X. Huang, Y. Chen, S.-L. Li, Y.-Q. Lan, Single-metal site-embedded conjugated macrocyclic hybrid catalysts enable boosted CO$_2$ reduction and evolution kinetics in Li-CO$_2$ batteries, Cell Rep. Phys. Sci. 2 (2021), 100583, https://doi.org/10.1016/j.xcrp.2021.100583.

[46] H. Kim, D. Shin, W. Yang, D.H. Won, H.-S. Oh, M.W. Chung, D. Jeong, S.H. Kim, K. H. Chae, J.Y. Ryu, J. Lee, S.J. Cho, J. Seo, H. Kim, C.H. Choi, Identification of single-atom Ni site active toward electrochemical CO$_2$ conversion to CO, J. Am. Chem. Soc. 143 (2021) 925–933, https://doi.org/10.1021/jacs.0c11008.

[47] Q. Fan, P. Hou, C. Choi, T.S. Wu, S. Hong, F. Li, Y.L. Soo, P. Kang, Y. Jung, Z. Sun, Activation of Ni particles into single Ni-N atoms for efficient electrochemical reduction of CO$_2$, Adv. Energy Mater. 10 (2019), 1903068, https://doi.org/10.1002/aenm.201903068.

[48] W. Ren, X. Tan, X. Chen, G. Zhang, K. Zhao, W. Yang, C. Jia, Y. Zhao, S.C. Smith, C. Zhao, Confinement of ionic liquids at single-Ni-sites boost electroreduction of CO$_2$ in aqueous electrolytes, ACS Catal. 10 (2020) 13171–13178, https://doi.org/10.1021/acscatal.0c03873.

[49] L. Lin, H. Li, C. Yan, H. Li, R. Si, M. Li, J. Xiao, G. Wang, X. Bao, Synergistic catalysis over iron-nitrogen sites anchored with cobalt phthalocyanine for efficient CO$_2$ electroreduction, Adv. Mater. 31 (2019), 1903470, https://doi.org/10.1002/adma.201903470.

[50] X. Yang, T. Tat, A. Libanori, J. Cheng, X. Xuan, N. Liu, X. Yang, J. Zhou, A. Nashalian, J. Chen, Single-atom catalysts with bimetallic centers for high-performance electrochemical CO$_2$ reduction, Mater. Today 45 (2021) 54–61, https://doi.org/10.1016/j.mattod.2021.01.011.

[51] Z. Chen, X. Zhang, W. Liu, M. Jiao, K. Mou, X. Zhang, L. Liu, Amination strategy to boost the CO$_2$ electroreduction current density of M-N/C single-atom catalysts to the industrial application level, Energy Environ. Sci. 14 (2021) 2349–2356, https://doi.org/10.1039/d0ee04052e.

[52] D.A.C. Brownson, D.K. Kampouris, C.E. Banks, Graphene electrochemistry: fundamental concepts through to prominent applications, Chem. Soc. Rev. 41 (2012) 6944–6976, https://doi.org/10.1039/c2cs35105f.

[53] Y. Yan, J. Miao, Z. Yang, F.-X. Xiao, H.B. Yang, B. Liu, Y. Yang, Carbon nanotube catalysts: recent advances in synthesis, characterization and applications, Chem. Soc. Rev. 44 (2015) 3295–3346, https://doi.org/10.1039/c4cs00492b.

[54] P. Trogadas, T.F. Fuller, P. Strasser, Carbon as catalyst and support for electrochemical energy conversion, Carbon 75 (2014) 5–42, https://doi.org/10.1016/j.carbon.2014.04.005.

[55] C.-X. Lü, G.-P. Zhan, K. Chen, Z.-K. Liu, C.-D. Wu, Anchoring Zn-phthalocyanines in the pore matrices of UiO-67 to improve highly the photocatalytic oxidation efficiency, Appl. Catal. B Environ. 279 (2020), 119350, https://doi.org/10.1016/j.apcatb.2020.119350.

[56] J. Sun, J. Bian, J. Li, Z. Zhang, Z. Li, Y. Qu, L. Bai, Z.-D. Yang, L. Jing, Efficiently photocatalytic conversion of CO$_2$ on ultrathin metal phthalocyanine/g-C$_3$N$_4$ heterojunctions by promoting charge transfer and CO$_2$ activation, Appl. Catal. B Environ. 277 (2020), 119199, https://doi.org/10.1016/j.apcatb.2020.119199.

[57] C. He, Y. Zhang, Y. Zhang, L. Zhao, L.-P. Yuan, J. Zhang, J. Ma, J.-S. Hu, Molecular evidence for metallic cobalt boosting CO$_2$ electroreduction on pyridinic nitrogen, Angew. Chem. Int. Ed. 59 (2020) 4914–4919, https://doi.org/10.1002/anie.201916520.